universe

MDPI

Article

Studying the Properties of Spacetime with an Improved Dynamical Model of the Inner Solar System

Dmitry Pavlov [1,*] and Ivan Dolgakov [2]

[1] Faculty of Computer Science and Technology, St. Petersburg Electrotechnical University, ul. Professora Popova 5, 197022 St. Petersburg, Russia
[2] Institute of Applied Astronomy RAS, Kutuzov Quay 10, 191187 St. Petersburg, Russia
* Correspondence: dapavlov@etu.ru

Abstract: Physical properties of the Sun (orientation of rotation axis, oblateness coefficient $J_{2\odot}$, and change rate of the gravitational parameter $\dot{\mu}_\odot$) are determined using a dynamical model describing the motion of the Sun, planets, the Moon, asteroids, and Trans-Neptunian objects (TNOs). Among the many kinds of observations used to determine the orbits and physical properties of the bodies, the most important for our study are precise interplanetary ranging data: Earth–Mercury ranges from MESSENGER spacecraft and Earth–Mars ranges from Odyssey and MRO. The findings allow us to improve the model of the Sun in modern planetary ephemerides. First, the dynamically determined direction of the Sun's pole is $\approx 2^\circ$ off the visible axis of rotation of the Sun's surface, which is corroborated by present knowledge of the Sun's interior. Second, the change rate of the Sun's gravitational parameter is found to be smaller (in absolute value) than the nominal value derived from the estimate of mass loss through radiation and solar wind. Possible interpretations are discussed.

Keywords: sun; radio astronomy; gravitational constant; planetary ephemerides

check for updates

Citation: Pavlov, D.; Dolgakov, I. Studying the Properties of Spacetime with an Improved Dynamical Model of the Inner Solar System. *Universe* **2024**, *10*, 413. https://doi.org/10.3390/universe10110413

Academic Editor: Costas Alissandrakis

Received: 30 September 2024
Revised: 30 October 2024
Accepted: 1 November 2024
Published: 3 November 2024

Copyright: © 2024 by the authors. Licensee MDPI, Basel, Switzerland. This article is an open access article distributed under the terms and conditions of the Creative Commons Attribution (CC BY) license (https://creativecommons.org/licenses/by/4.0/).

1. Introduction

Since the beginning of radio astronomy and laser ranging, the precise determination of orbits has played an important role in geophysical studies of Solar system bodies and tests of General Relativity. One of such tests is the estimation of the possible change rate of gravitational constant G. Such an estimation cannot be performed by directly measuring G at different times because of the low accuracy of direct measurement via classical torsion balance: the current best estimate has the relative standard uncertainty of 2.2×10^{-5} [1]; also, some modern measurements have a relative difference of about 5×10^{-4}, which is hypothesized to come from currents in the Earth's fluid core [2].

Early attempts to estimate $\dot{G}$ relied on radar ranging of planets and spacecraft radio ranging (see e.g., refs. [3–5]). As more observations become available, more complex and detailed models of the motion of the Solar system bodies and astrometric reductions are required to adequately represent the observations and infer scientific information. This work is a continuation of [6], where constraints on $\dot{G}$ were obtained within the framework of the planetary ephemerides EPM. Since then, several improvements have been made: a new solar plasma delay model [7] based on in situ electron density data; the use of a priori values of asteroid masses based on observed diameters [8]; an updated rotation axis of the Sun (presented in this work). The improvements have allowed us to revisit the previously obtained results. Key observational data for this study are range points (hereinafter "ranges") between DSN stations on Earth and the center of Mercury and Earth–Mars ranges obtained from MGS, Mars Odyssey, and MRO. Each range point is a pseudo-observation of the radio delay between the station and the center of the planet. It is formed from raw observations acquired during one tracking pass, whose systematic errors are strongly correlated.

The estimation of $\dot{G}$ is performed via the estimation of the change rate of the solar gravitational parameter $\mu_\odot$ (see Section 6.3), which is naturally negative because of the solar wind and energy lost by the Sun. The orbits of Mercury, Earth, and Mars are affected by $\dot{\mu}_\odot$ in a measurable way. However, since $\dot{\mu}_\odot$ manifests itself only via a slight change in the force of gravity, other factors affecting the force of gravity must be accounted for, most notably the value of $\mu_\odot$ itself and the solar oblateness factor ($J_{2\odot}$); they are both estimated as well. A precise estimation of $\mu_\odot$ poses a challenge because this parameter is correlated with the semi-major axes of planetary orbits, which, in turn, are correlated with transponder delays of spacecraft (see Section 2.1). Ranges to Jupiter and Saturn are of help, as they put additional constraints on the parameters of the orbit of the Earth (although introducing their own transponder delays). On a different note, the orbits of the inner planets and Jupiter are affected by hundreds of asteroids. The orbits of asteroids must be modeled and their masses (see Section 3.1) must be either estimated from ranges[1], or known with good accuracy from other techniques.

We also must model the Lense–Thirring effect (see Section 3.3) because it affects the orbit of Mercury enough to interfere with the determination of $\dot{\mu}_\odot$. Finally, the orbit of the Earth is affected by the orbit of the Moon, which, in turn, is sensitive to $\mu_\odot$ and $J_{2\odot}$; in order to reduce systematic errors in the processing of interplanetary ranges, we model the motion of the Moon together with the Sun, planets, and asteroids, and fit the parameters of orbit and physical libration of the Moon to lunar laser ranging (LLR) observations.

In the following sections, we describe the data and models used and present results of numerical experiments obtained via the fitting of free parameters to the whole set of astrometrical data.

2. Data

2.1. Observations

MESSENGER data were obtained from the webpage of Solar System Dynamics (SSD) group at NASA JPL[2], as were the ranging data from MGS, Mars Odyssey, and MRO [9], ranging and differenced range data from Viking [10] and Pathfinder [11], and older radar data. Mars Express ranges [12] were downloaded from the Geoazur website[3]. Radar ranging data from Crimea were available on the IAA RAS website[4].

While this work is focused on subtle effects visible in Earth–Mercury and Earth–Mars ranges, all massive bodies in the Solar system affect each other; Earth, Sun, Mercury, and Mars must be treated as part of the dynamical system involving all the planets, significant asteroids, and Trans-Neptunian objects; also, due to the orbit of the Earth being significantly dependent on the orbit of the Moon, it must be present too, on par with the Sun and the planets. Venus Express data were taken from the aforementioned Geoazur website; ranges to Juno and Cassini orbiters were obtained from the aforementioned SSD website. LLR data from observatories in Apache Point [13–15] (NM, USA), Matera (Italy), Grasse [16] (France), and Wettzell [17] (Germany) were obtained from CDDIS[5], while historical observations from McDonald/MLRS1/MLRS2 [18] and Haleakala [19] observatories, as well as older data for Grasse (Ruby and YAG [20] lasers) were downloaded from POLAC[6].

Optical observations for outer planets and their satellites were used to constrain the orbits of outer planets in the planetary solution. Also, a limited number of "3D normal points" of spacecraft flybys were used. Finally, VLBI observations of planetary orbiters were used to tie the Solar system to the celestial frame. Those observations are largely the same as were used in EPM2021 ephemeris and previous versions of EPM; for details, we refer the reader to [21–24], and references therein.

While the observations widely differ by time, instrument, team, observed body, kind of observed value (range or angular coordinates), and accuracy, they were all processed in a single dynamical model of the Solar system (see Section 3). Each observation was assigned a weight according to its accuracy, and a model value that was calculated from the parameters of planetary orbits and other parameters. First-order derivatives were calculated of all observations with respect to parameters they were sensitive to, and then

the parameters were fit to minimize the weighted least square difference between the model values and the actual observed values (see Section 4).

2.2. Other Data

Orbital parameters of asteroids and TNOs were taken from JPL Horizons online service.[7]

A priori values based on diameters observed in the infrared [25,26] were used in the dynamical estimation of masses of asteroids and TNOs that could not be determined from precise techniques.

The EOP series required for astrometric reductions were obtained from the IERS website[8]. The DSN stations' coordinates were taken from the aforementioned SSD website.

3. Dynamical Model

3.1. Bodies and Their Gravity

The dynamical model used in this work was for the most part described in multiple papers dedicated to EPM ephemerides (see, e.g., ref. [24] and references therein). All bodies present in the model were numerically integrated simultaneously. The numerical integration was performed via an Adams–Bashforth–Moulton predictor-corrector scheme of order 13 with the time step of 1.5 h. A modification of the scheme was carried out so as to handle the time-delayed terms in the dynamical equations of the rotation of the Moon [27].

The list of bodies included the Sun, the Moon, the planets, selected asteroids and TNOs, as well as the discrete uniform 180-point annulus, approximating the gravitational action of the remaining asteroids, and the discrete uniform 160-point annulus, approximating the gravitational action of the remaining TNOs. The total number of individual asteroids was 249, which is less than 277 in [24], because some more asteroids were removed whose masses were determined to be negative (always within uncertainty).

The masses of only 17 asteroids are known with good accuracy because they are either binary asteroids (e.g., Kalliope) or had spacecraft orbiting them (e.g., Ceres). The masses of some other asteroids are estimated by deflections of other asteroids' orbits on approach (e.g., Iris), though estimates may differ across works. The masses of the remaining asteroids were determined dynamically in the planetary solution, with a priori values based on observed diameters and taxonomic classes [8].

The gravitational parameter of the discrete TNO annulus was fixed to 8.847×10^{-12} au^3/day^2 (which is close to 9.848×10^{-12} from [28]). The gravitational parameter of the discrete asteroid annulus was determined dynamically.

Most bodies were modeled as point masses interacting either with Newtonian forces or (for the sixteen most important bodies) following the Einstein–Infeld–Hoffmann equations of motion. For the Earth and the Moon, a non-spherical gravitational potential up to degree and order 6 was modeled, together with the elasticity and liquid core of the Moon, and lunar and terrestrial tides [29]. Effects that are of particular importance in this work are described in the further subsections.

3.2. Acceleration from Solar Oblateness

$$\mathbf{a}_i^{(\mathrm{obl})} = 3J_{2\odot}\mu_\odot \frac{R^2}{r_{i\odot}^4}\left\{\left[\frac{5}{2}\left(\frac{\mathbf{r}_{i\odot}}{r_{i\odot}}\cdot\mathbf{p}\right)^2 - \frac{1}{2}\right]\frac{\mathbf{r}_{i\odot}}{r_{i\odot}} - \left(\frac{\mathbf{r}_{i\odot}}{r_{i\odot}}\cdot\mathbf{p}\right)\mathbf{p}\right\}, \quad (1)$$

where $\mathbf{p}$ is a unit vector directed at the Sun's north pole. In previously released versions of EPM, the direction was taken according to the rotational parameters of the Sun accepted by the IAU and derived from the visible motion of the sunspots:

$$\mathbf{p} = \mathrm{R_z}(\alpha_0 - 270^\circ)\mathrm{R_x}(90^\circ - \delta_0)\mathbf{z}, \quad (2)$$

where $\mathbf{z} = (0\ 0\ 1)^T$, $\alpha_0 = 286.13$, $\delta_0 = 63.87$ (see, e.g., ref. [30]). The same approach was taken in DE [31], INPOP [32], and PETREL [33] ephemerides. While the values of α_0

and δ_0 are probably accurate, we should not assume that the sunspots and the interior regions of the Sun rotate around one common axis. In this work, the angles α_0^* and δ_0^* (still defining a common rotation axis, but not necessarily coincident with the "visible" one) were determined as solution parameters. As for $J_{2\odot}$, while it has been determined by helioseismic inference of internal rotation in [34] to be $(2.21 \pm 0.01) \times 10^{-7}$ (3σ), it was nevertheless made a solution parameter in this work in order to verify this finding via dynamics.

3.3. Lense–Thirring Effect

The rotational frame-dragging effect in the gravitational field of a rotating massive body causes the orbits of objects around that body to precess. This effect, predicted by General Relativity and first derived in [35], has been notably hard to observe to this day. One indisputably successful test has been the Gravity Probe B mission [36,37] (an Earth satellite), which confirmed the effect with an accuracy of 19%; however, it did not measure the precession of the spacecraft's orbit but rather the precession of the spin axis of a freely moving gyroscope; such a test was first proposed in [38,39].

The Lense–Thirring acceleration can be formulated as follows [40]:

$$\mathbf{a}_i^{(\mathrm{LT})} = \frac{2}{c^2} G S_\odot \frac{1}{r_{i\odot}^3} M_\odot \left(\dot{\mathbf{r}}_{\mathbf{i}\odot} \times \mathbf{p} + 3 \frac{\mathbf{p} \cdot \mathbf{r}_{\mathbf{i}\odot}}{r^2} \mathbf{r}_{\mathbf{i}\odot} \times \dot{\mathbf{r}}_{\mathbf{i}\odot} \right), \tag{3}$$

where $S_\odot$ is the angular momentum of the Sun. Since the launch of the second LAGEOS satellite, test were conducted to confirm the Lense–Thirring acceleration in the gravitational field of the Earth, see, e.g., ref. [41], where an accuracy of 10% was reported, or a later work [42] with a reported improved accuracy of 2%; however, there is an ongoing debate about the correctness of that methodology, see, e.g., refs. [43–46].

It was hoped that the Juno spacecraft, thanks to its polar orbit, would allow to test the Lense–Thirring effect via an estimation of the angular momentum of Jupiter [47,48], but it did not work out with the actual measurements [49].

Possibilities for measurements of the Lense–Thirring effect from planetary dynamics, including the MESSENGER mission, were explored in [50,51]. It was later shown in [52–54] that it is not possible at present to overcome the strong anticorrelation between $S_\odot$ and $J_{2\odot}$ in Earth–Mercury ranges. The numerically estimated anticorrelation was 92%. The present accuracy of the non-dynamical determination of $J_{2\odot}$ (see Section 3.2) allows for an estimation of $S_\odot$ from MESSENGER observations with an accuracy of 25% [52]. The data from the extended phase of the BepiColombo mission is expected to improve this result [55]. In our model, we fixed $S_\odot$ to the value inferred from helioseismology in [56]: 190×10^{39} kg/m^{2}s.

3.4. Sun Mass Loss Rate

In this work, the gravitational parameter of the Sun was assigned a linear trend:

$$\mu_\odot(t) = \mu_\odot^{(0)} + \dot{\mu}_\odot \cdot (t - t_0), \tag{4}$$

where the epoch t_0 was chosen to be JD 2454000.5 (22 September 2006) so that it was within the timespan of the precision ranging observations used in the solution: from the beginning of MGS data in 1999 till the end of available Odyssey and MRO data in 2017; MESSENGER ranges began in 2011 and ended in 2014.

The nominal value of $\dot{M}_\odot$ is made up of radiation and solar wind terms (the normalized form is given):

$$\frac{\dot{M}_\odot}{M_\odot} = \frac{\dot{M}_\odot^{\mathrm{rad}}}{M_\odot} + \frac{\dot{M}_\odot^{\mathrm{wind}}}{M_\odot} \tag{5}$$

The mass loss rate due to radiation was derived from the IAU nominal value of solar radiation: $\mathcal{L}_\odot^{\mathrm{N}} = 3.828 \times 10^{26}$ W [57], which gives

$$\dot{M}_\odot^{\mathrm{rad}} / M_\odot = -\mathcal{L}_\odot^{\mathrm{N}} / (M_\odot c^2) = -2.142 \times 10^{-21}\ \mathrm{s}^{-1} = -6.760 \times 10^{-14}\ \mathrm{yr}^{-1}. \quad (6)$$

The actual value is known to be fluctuating; depending on the period, the estimates of amplitude of fluctuations are 0.2% for a 27-day rotation period and 0.1% for an 11-year solar cycle [58]. On secular timescales, the estimate is about 0.11% [59]. If we take the IAU-compliant value as the average, we can be sure that the error of this average is lower than the fluctuations, and obtain a safe margin of error $-6.77 \times 10^{-14} < \dot{M}_\odot^{\mathrm{rad}} / M_\odot < -6.75 \times 10^{-14}$.

Mass loss due to the solar wind is harder to observe or estimate due to its significant variation in both latitude and time, and the non-perfection of solar wind models. Years of interest (1999–2017) were within solar cycles 23 (1996–2008) and 24 (2008–2019). Estimates in [60] based on *Wind*'s measurements concluded that the average value was "$2.1 \times 10^{-14}\ M_\odot\ \mathrm{yr}^{-1}$ for cycle 23 and decreases by around 10% for cycle 24". Estimates in [61], based on OMNI data (combined from measurements from ACE and *Wind* spacecraft) and Ulysses measurements, were in a similar range for the said timespan and were confirmed by a model. Estimate in [6] for $\dot{M}_\odot^{\mathrm{wind}} / M_\odot$ was in the range from -6.6×10^{-14} to -3.0×10^{-14}. This estimate was based solely on the Ulysses data (SWOOPS) in its entire operating interval (1990–2008). Ulysses estimates shown in [61] seemed to confirm the -3.0×10^{-14} average value but only thanks to the high (above 3×10^{-14}) mass loss rate in the early 1990s, which was outside our timespan of interest; after 1999, an average mass loss rate of about 2×10^{-14} seemed very plausible. As a counterpoint, a model in [62] gave the value of 4.1×10^{-14} for a particular solar maximum (CR 2159, January 2015), which was not confirmed in [61].

Solar mass is also lost to CMEs; however, CMEs account for no more than 10% of the mass loss as compared to solar wind [60,63]. Considering all of the above, and accounting for possible error due to variations in latitude (direct observations of solar wind outside ecliptic have not been made since 2008), we used the following safe bounds of mass loss rate due to solar wind and CMEs in 1999–2017: $-3.1 \times 10^{-14} < \dot{M}_\odot^{\mathrm{wind}} / M_\odot < -1.9 \times 10^{-14}$, with the nominal value of -2.1×10^{-14}.

Combining all of the above, we obtained the nominal value

$$\dot{M}_\odot / M_\odot \approx -8.9 \times 10^{-14}\ \mathrm{yr}^{-1} \quad (7)$$

and the safe bounds

$$-9.9 \times 10^{-14}\ \mathrm{yr}^{-1} < \dot{M}_\odot / M_\odot < -8.6 \times 10^{-14}\ \mathrm{yr}^{-1} \quad (8)$$

4. Processing of Observations

The full set of planetary parameters was fitted via the Gauss–Newton method to the full set of planetary observations (Section 2.1). The set of planetary parameters of EPM2021 was taken, including the following:

- Initial parameters of orbits of planets (at the epoch given in Section 3.4) in the reference plane of Earth's mean equator at epoch J2000.
- Masses of asteroids (see again Section 2.1);
- $\mu_\odot$ was determined via the scaling factor (correction to the value of astronomical unit) in EPM2021 but was determined directly in this work;
- μ_{annulus} of the 180-point discrete asteroid annulus;
- The Earth/Moon mass ratio;
- $J_{2\odot}$;

- Transponder delays for planetary orbiters and landers (while transponders are calibrated on Earth, this calibration is not precise enough and/or breaks in the conditions of outer space, so the additional delay must be determined, either positive or negative);
- One factor of solar plasma delay [7];
- Two sets of biases for DSN stations [64]: one for MGS and Odyssey spacecraft, the other for the MRO spacecraft.

The listed parameters affect precision ranges to orbiters of inner planets. Other parameters were also determined in the planetary solution that were not directly important for this work: corrections to various systematic effects of earlier observations of planets and Martian landers, angles of orientation of the ephemeris frame to ICRF, etc.

An important detail is that MESSENGER ranges, unlike those of Martian spacecraft, are provided only in the form with the solar plasma delay subtracted from them according to a model developed by NASA JPL. Without knowing that model in detail, we cannot be sure that no systematic effects remain in the data that could in principle affect the results of this work. Ironically, as said in [65], "mission's published science objectives [66] do not include determination of PPN parameters or J_2 of the Sun. MESSENGER is equipped with only one radio link (X-band)". That decision rendered impossible a reliable technique to determine solar plasma delay (Differenced Range Versus Integrated Doppler [67]); and the JPL model of solar plasma delay has proven not to be the most accurate in some cases [7].

Additional parameters were included in some of the solutions described in further sections: the α_0^* and δ_0^* angles of the Sun's rotation axis and $\dot{\mu}_\odot$.

Parameters of the Earth–Moon system and the geocentric orbit of the Moon were determined in a separate solution (lunar) according to the JPL DE model; for details, we refer to [23,29] and references therein. Planetary and lunar solutions in this work were obtained iteratively in an interleaving manner, so that the lunar solution accounted for the perturbations brought by the changes in planetary solution (most notably change in $\mu_\odot$), and the planetary solution, in turn, benefited from a more correct orbit of the Moon (and hence a more correct orbit of the Earth).

5. Experiment and Results

Three solutions were obtained:

I With fixed α_0 and δ_0 and nominal $\dot{\mu}_\odot$;
II With determined α_0^* and δ_0^* and nominal $\dot{\mu}_\odot$;
III With determined α_0^*, δ_0^*, and $\dot{\mu}_\odot$.

Selected parameters determined in the three solutions are listed in Table 1, while selected one-way wrms are listed in Table 2. Model differences in MESSENGER ranges between the three solutions are shown on Figures 1–3. MESSENGER range residuals for Solution III are shown in Figure 4.

Table 1. Comparison of parameters for the solutions I, II, and III. The uncertainty was 3σ.

Parameter	Solution I	Solution II	Solution III
$\mu_\odot^{(0)} - 295912208283$, $\frac{\text{au}^3}{\text{day}^2} \times 10^{-15}$	0.78 ± 0.27	0.37 ± 0.27	0.51 ± 0.27
$J_{2\odot}$, 10^{-7}	2.208 ± 0.021	2.199 ± 0.021	2.198 ± 0.021
Solar plasma delay factor	1.102 ± 0.033	1.106 ± 0.033	1.112 ± 0.033
MESSENGER transponder delay, m	-1.91 ± 0.30	-1.82 ± 0.30	-1.83 ± 0.31
$\dot{\mu}_\odot/\mu_\odot$, $\text{yr}^{-1} \times 10^{-14}$	fixed to -8.9	fixed to -8.9	-3.4 ± 3.1
α_0^*, $^\circ$	fixed to 286.13	287.72 ± 1.32	287.86 ± 1.32
δ_0^*, $^\circ$	fixed to 63.87	61.86 ± 0.78	61.98 ± 0.78

Table 2. One-way wrms values for solutions I, II and III.

Observation Group	No. of Ranges	Solution I	Solution II	Solution III
MRO	1924	0.617 m	0.618 m	0.620 m
MGS	5590	0.921 m	0.921 m	0.922 m
Odyssey	7988	0.565 m	0.565 m	0.565 m
MESSENGER	1141	0.669 m	0.652 m	0.647 m

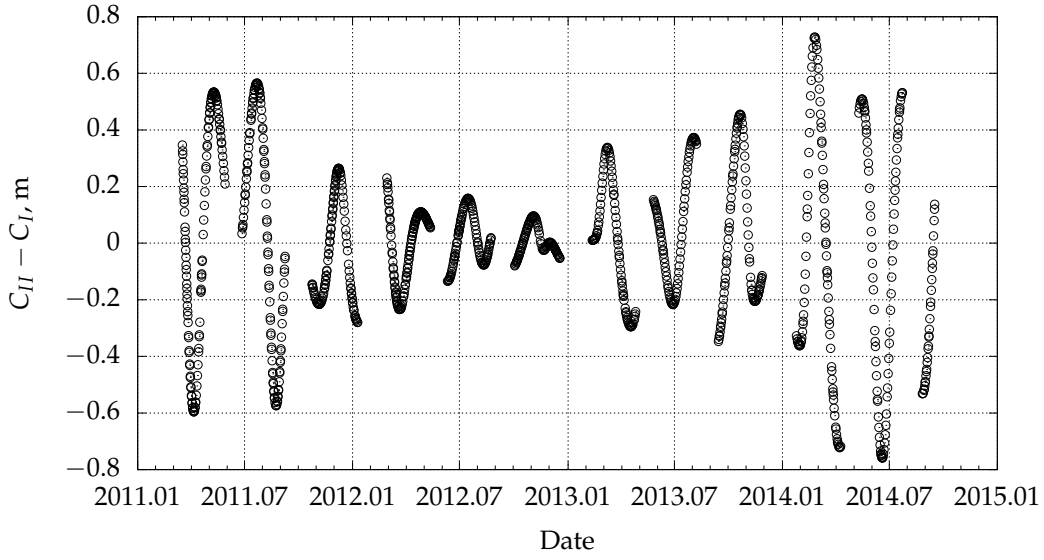

Figure 1. Difference between model values of MESSENGER ranges ($C_{II} - C_I$).

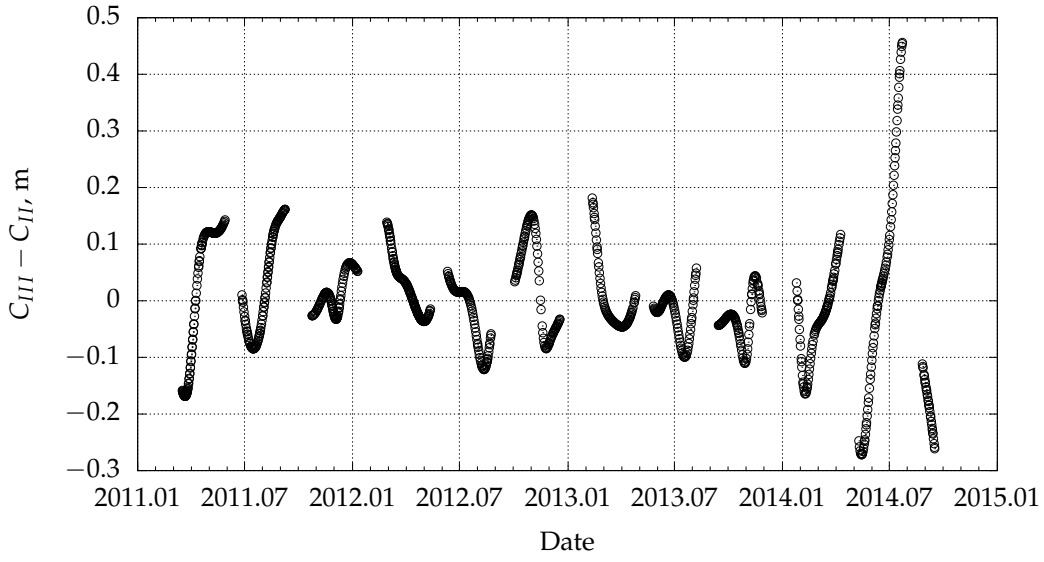

Figure 2. Difference between model values of MESSENGER ranges ($C_{III} - C_{II}$).

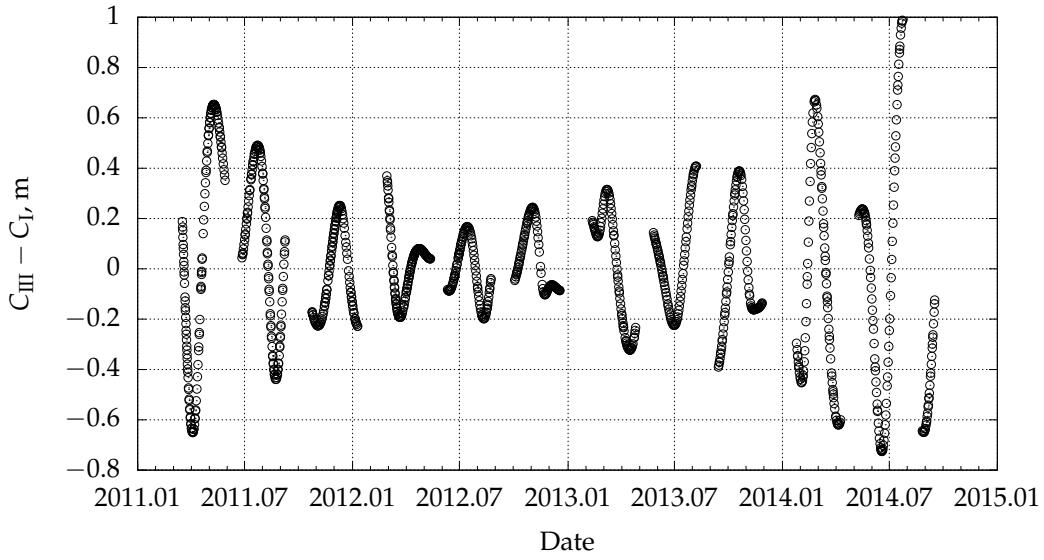

Figure 3. Difference between model values of MESSENGER ranges ($C_{III} - C_I$).

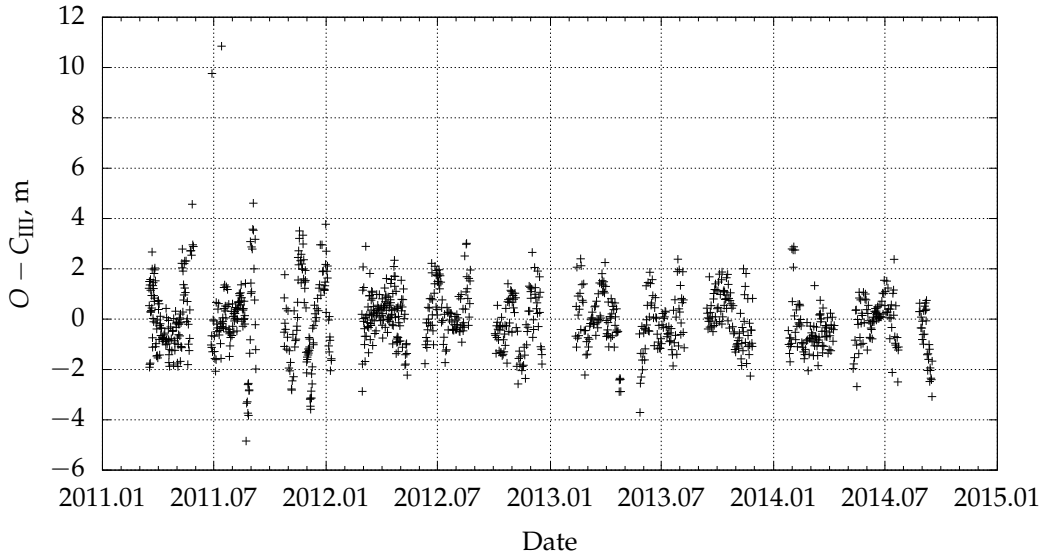

Figure 4. MESSENGER residuals $O - C_{III}$.

6. Discussion

6.1. Comparison Between Solutions

The determined $J_{2\odot}$ values in all three solutions were in good agreement with the helioseismology value of $(2.21 \pm 0.01) \times 10^{-7}$ [34]. The introduction of α_0^* and δ_0^* angles as fitted parameters improved the MESSENGER wrms by 17 mm (or about 15 cm in the root-mean-square sense); the further introduction of $\dot{\mu}_\odot$ as fitted parameter improved the MESSENGER wrms by 5 mm (or 8 cm in the root-mean-square sense).

6.2. Solar Rotation Axis

The determined α_0^* was different from the nominal α_0 by more than three estimated standard deviations, and δ_0^* was different from the nominal δ_0 by more than three estimated standard deviations plus 1°. The dynamically determined rotation axis of the Sun was notably different from the observed one. While the nominal orientation $R_z(16.13)R_x(26.13)$ in the equatorial system gave the solar equator inclined 7.25 to the ecliptic, the determined orientation gave the inclination of 8.98 (Solution II) or 8.91 (Solution III). The azimuths of the two rotation axes (with respect to the ecliptic) differed by 8.94 (Solution II vs. Solution I)

or by 7.69 (Solution III vs. Solution I). These numbers are within the 1.5σ confidence level of the "mean pulsation axis" estimates in [68] obtained from the analysis of LOI measurements on SOHO. Also, our finding is consistent with the existence of a hypothetical inner region of the Sun ("core") that rotates differently than the envelope (in [69], this was assumed from the analysis of solar flares). Even so, we emphasize that the "rotation axis" determined within our model is not a real rotation axis of any part of the Sun, but merely an averaged approximation of how two different effects (solar oblateness and Lense–Thirring effect) jointly act in the case of a non-axially symmetric body. It is an open question whether it is possible to study the Sun's interior by planetary dynamics via a more physically correct analysis, separating solar oblateness effect from the Lense–Thirring effect.

6.3. Apparent Change of the Gravitational Constant

Introducing the hypothetical change rate of the gravitational constant G:

$$\frac{\dot{\mu}_\odot}{\mu_\odot} = \frac{\dot{M}_\odot}{M_\odot} + \frac{\dot{G}}{G}, \tag{9}$$

and taking the safe (3σ) bounds for $\dot{\mu}_\odot$ obtained in Solution III:

$$-6.5 \times 10^{-14}\ \mathrm{yr}^{-1} < \frac{\dot{\mu}_\odot}{\mu_\odot} < -0.3 \times 10^{-14}\ \mathrm{yr}^{-1}, \tag{10}$$

and taking into account the safe bounds for $\dot{M}_\odot$ (8), we obtained the following constraints for $\dot{G}$:

$$2.0 \times 10^{-14}\ \mathrm{yr}^{-1} < \frac{\dot{G}}{G} < 9.6 \times 10^{-14}\ \mathrm{yr}^{-1} \tag{11}$$

These bounds are within most of the earlier obtained bounds for $\dot{G}$ by non-dynamical methods:

- $(1.2 \pm 2.6) \times 10^{-12}$ in [70] by the seismology of an ancient star;
- $(3.6 \pm 4.5) \times 10^{-12}$ in [71] by CMB observations;
- $(1 \pm 9) \times 10^{-13}$ in [72] by the timing of a single pulsar;
- $(0 \pm 2) \times 10^{-13}$ in [73] by helioseismology;
- $(5.3 \pm 6) \times 10^{-14}$ in [74] by observations of adsorption lines in quasar spectra.

However, in later work [75] the bounds obtained by quasar spectra were tightened to $(0.92 \pm 2.83) \times 10^{-15}$, which is not compatible with values found in this work.

Other estimates of $\dot{\mu}_\odot$ are known, derived from MESSENGER ranges. The first work of the kind [53] involved processing of raw radio science data and the integration of the orbit of MESSENGER around Mercury, rather than using the range points provided by JPL, as in other works. It is not clear which model of solar plasma delay was used. Only Mercury's orbit was fitted; the orbits of other planets were taken from a JPL DE ephemeris. The obtained estimate was $\dot{\mu}_\odot/\mu_\odot = (-6.13 \pm 4.41) \times 10^{-14}$ (3σ), which largely intersects with our estimate (10) but, unlike the latter, allows zero $\dot{G}$.[9]

Another estimate based on MESSENGER is given in [32]: $\dot{\mu}_\odot/\mu_\odot = (-3.7 \pm 3.2) \times 10^{-14}$ (3σ), which is close to our estimate (10). However, no conclusion about hypothetically positive $\dot{G}$ was made because the account of the Sun's mass loss rate $\dot{M}_\odot/M_\odot = (-9.2 \pm 6.1) \times 10^{-14}\ \mathrm{yr}^{-1}$ (3σ) was taken as a compromise between [76,77]. Neither paper is relevant to the timespan of MESSENGER observations; moreover, the margin of error was too wide because of the said compromise.

Another approach undertaken in [32] was the WRSS filtering, which is more conservative than the least squares fitting used in this and other works. The obtained estimate was $\dot{\mu}_\odot/\mu_\odot = (-1.03 \pm 2.28) \times 10^{-13}$, which rendered the estimates of $\dot{G}/G$ at the 10^{-14} level impossible.

All in all, we should not infer right away that the positive $\dot{G}$, found in Solution III, indicates a secular change in G in the whole Universe. We may instead suppose that it is an *apparent* change in $\dot{G}$ that comes from either:

- An inaccurate modeling of the solar plasma delay of MESSENGER ranges. As said above, the ranges provided by NASA JPL and used in this work have the solar plasma delay subtracted from them; in [53], a custom procedure of processing the raw radio science data was used, but the details of the solar plasma model are not clear. Possible systematic errors in the solar plasma delay model, which are in the scale of meters, surely can interfere with the processing of MESSENGER ranges whose residuals are in the scale of decimeters.
- An inaccurate modeling of the asteroid belt. While the present model does a good job representing the "generic" part of the belt by 180 uniformly distributed point-masses [78], there is no certainty that no systematic errors remain. Work is underway to make an improvement of the asteroid belt modeling in INPOP ephemerides [79]. Also, it is important to note that the present procedure of individual asteroid masses' determination [8] does not disallow negative masses; they are excluded from the solution in an ad hoc manner, while in principle, a dedicated method (BVLS) should be applied.
- An unmodeled change in $J_{2\odot}$. Solar gravitational moments are known to have temporal variations over a solar cycle, including $J_{2\odot}$. The helioseismological estimate made in [80] was 1.0×10^{-10} in amplitude per 11 years. A numerical experiment (not included here) showed that a change in $J_{2\odot}$ by 2.0×10^{-10} over 6.5 years ($\dot{J}_{2\odot}/J_{2\odot} \approx 0.014\%\ \mathrm{yr}^{-1}$) resulted in a notable signature in Earth–Mercury ranges, reaching 40 cm in amplitude, which is well comparable to the MESSENGER residuals. However, little is presently known about the phase of a possible $J_{2\odot}$ oscillation during solar cycles 22 and 23, or possible higher-frequency oscillations. This issue requires further research.
- Some local effect in the spacetime of the Solar system, rather than in the whole Universe or remote quasars. The hypotheses about such effects are outside the scope of this paper.

Some other systematic effects that are less believed to affect the results are given in Sections 6.4–6.6.

6.4. Fall of Mass into the Sun

Let us consider a positive $\dot{M}_{\odot}^{\mathrm{fall}}$ due to comets, asteroids, and interplanetary dust falling into the Sun. Such effects, in principle, would move the estimated range of $\dot{G}$ to the left.

The comets that come in closest proximity to the Sun (sungrazers) have been observed by the SOHO space observatory since 1995, currently numbered in the thousands. Such comets rarely survive perihelion passage; however, the most frequent outcome is total evaporation of the comet before it reaches the surface, after which the small particles are pushed outwards by the solar pressure. A comet actually fallen into the Sun is a rare event; but even if 100 comets, each 1 km in radius, fell into the Sun in a year, the resulting mass acquisition relative rate would be less than 1×10^{-18}, a negligible value compared to the mass loss by radiation and solar wind. The mass acquisition rate due to the fall of the interplanetary dust is also considered negligible, less than $1 \times 10^{-17}\ M_{\odot}\mathrm{yr}^{-1}$, see [6].

Asteroids, unlike comets, have no record of falling into the Sun, while calculations show that such events can happen on a million-year timescale [81]. For this effect to be noticeable in our studies (say $1 \times 10^{-15}\ M_{\odot}\mathrm{yr}^{-1}$ of acquired mass), 90 asteroids, each 20 km in diameter, of the most dense type (5.3 $\mathrm{g/cm}^3$) should fall into the Sun per year, and not fall apart and be pushed out by solar pressure like most comets.

We could imagine that some small asteroids do fall into the Sun unnoticed; in that case, they should come from what is modeled as the 180-point annulus, a gravitational equivalent of all asteroids that are not in the model individually. The $\mu_{\mathrm{annulus}}/\mu_{\odot}$ was

determined dynamically to be ≈3.4 $\times 10^{-11}$ in EPM2021 [82] and ≈5.7 $\times 10^{-11}$ $M_\odot$ in this work. If some 1×10^{-15} $M_\odot$ of asteroids (per year) were to leave the annulus to fall into the Sun in modern times, it would have meant that we happened to be close, on astronomical timescale, to witnessing the waning of the asteroid belt (with the exception of large asteroids). As such a circumstance is unlikely, we must conclude that $\dot{M}_\odot^{\text{fall}}$ is negligible in our study.

One could argue that the population of small asteroids is replenished by collisions between small and big asteroids. However, the estimates of the asteroid collision probabilities [83] are nowhere near levels required for tens of collisions in a year.

For the sake of completeness, it must be noted that an asteroid does not have to fall into the Sun to increase the apparent $M_\odot$; asteroids on hypothetical orbits inside the orbit of Mercury (vulcanoids) would have produced similar gravitational effect. However, the population of vulcanoids is decreasing rather than increasing, if it exists at all [84].

6.5. Change of $S_\odot$

The Sun is slowly losing its angular momentum because of the torque exerted by its magnetic field interacting with solar wind. This effect has been studied since 1967 [85]. The estimation of its amount requires estimating both the mass loss due to solar wind and the Alfvén radius; the latter in turn requires the estimation of the open magnetic flux. In [86], the average angular momentum loss rate was found to be 2.2×10^{30} erg—both secular and since 2000, and in the latter case, the in situ measurements from the OMNI dataset were used to estimate the open magnetic flux. In [87], based only on the *Wind* spacecraft measurements, the average momentum loss was estimated to be 3.3×10^{30} erg.

According to [88], the secular change in the semi-major axis a of a planet due to Sun's momentum loss rate $\dot{S}_\odot$ is:

$$\langle \dot{a} \rangle = 4 \frac{G\dot{S}_\odot}{c^2 \sqrt{\mu_\odot a}} \cos \varepsilon, \tag{12}$$

where ε is the obliquity of the ecliptic. Using the value of 3.3×10^{30} erg for $\dot{S}_\odot$, we obtain the secular change in the semi-major axis of Mercury $\langle \dot{a} \rangle \approx -1 \times 10^{-11}$ m/yr, which is negligible for our study. Secular variations in other orbital elements in [88] are of similar order.

6.6. Gravitational Wave Background

Low-frequency gravitational waves were recently confirmed by pulsar timing [89]; however, the reported strain amplitudes were on the order of 10^{-14}, which is too small to be detected by precision radio ranging (less than 1 mm change in Earth–Mercury distance).

7. Determining $\dot{G}$ in Lunar Solution

An attempt was made to determine $\dot{G}$ in the lunar solution. Obviously a finite $\dot{G}$ would cause a trend to the gravitational parameter of the Earth–Moon system μ_{EM}, and LLR data, accumulated over more than half a century, are very sensitive to this parameter. Moreover, in the case of the Earth–Moon system, it is much easier to extract $\dot{G}$ from $\dot{\mu}$. The flux of meteoroids falling onto the Earth and the Moon is estimated to be less than 2.8×10^{-18} $M_\oplus$ [90]. As for the solar wind, even assuming that all its particles that reach the Earth magnetosphere are completely consumed, it would be less than 5×10^{-8} of the overall flux. Using the nominal value of $\dot{M}_\odot^{(\text{wind})} = -2.1 \times 10^{-14}$ $M_\odot$, we would obtain $\dot{M}_{\text{EM}}^{(\text{wind})} < 1.05 \times 10^{-21}$ $M_\odot < 3.5 \times 10^{-16}$ M_{EM} yr^{-1}. In that case, the solar wind acquisition would dominate the meteoroids' acquisition but would be still be negligible.

Unfortunately, as was already reported in [54], $\dot{\mu}_{\text{EM}}$ cannot be reliably estimated in the lunar solution because it is hard to separate from two parameters of Earth tides, namely, the rotational delays of the Earth's diurnal and semi-diurnal tides [91]. The correlation of $\dot{\mu}_{\text{EM}}$ with τ_{1R} and τ_{2R} is 91.7% and 99.6%, respectively. Alternatively, the IERS tidal model [40]

does not need to be fit to LLR observations, but it does not provide as good a fit as the DE tidal model [23,29]. More research on Earth tides is needed before estimating $\dot{G}$ via LLR.

8. Conclusions

- The solar equator orientation angles, used in EPM and other ephemerides to this day to model acceleration from solar oblateness and the Lense–Thirring effect (in ephemerides where it is modeled), have no legitimate reason to be used for that purpose. The internal structure of the Sun is complex and there is no common rotation axis. An experiment showed that even a slight update to the model—keeping the single dynamical solar rotation axis but allowing it to differ from the "visible" one—significantly improved the modeling of MESSENGER ranges. It remains an open question whether more accurate modeling is possible.
- $\dot{\mu_\odot}$ was determined from the whole set of planetary observations, including MESSENGER, to $(-3.4 \pm 3.1) \times 10^{-14}\ \mu_\odot/\mathrm{yr}$ (3σ). This, in turn, allowed us to estimate the time variation in the gravitational constant: $2.0 \times 10^{-14}/\mathrm{yr} < \dot{G}/G < 9.6 \times 10^{-14}/\mathrm{yr}$.
- The positive value of $\dot{G}$ may not be real but apparent, owing to the imperfection of the models of solar plasma delay, asteroid belt, change in $J_{2\odot}$. Less likely but possibly, it may indicate some local effect in the spacetime of the Solar system in 2011–2014.
- Care must be taken in research to properly estimate the mass loss of the Sun to the solar wind. The most modern models, and in situ observations made during the studied timespan, must be used. The model of solar plasma delay is also very important in research based on precise planetary radio ranges.
- Also, the variation in $J_{2\odot}$ is an important effect for the dynamics of Mercury, and a theory should be proposed in the future for the modeling of this effect.
- Updated data can help to improve or disprove the $\dot{G}$ estimate obtained in this work: MESSENGER ranges without the solar plasma delay subtracted and MRO and Odyssey ranges past 2017.
- Future Earth–Mercury ranges produced from the BepiColombo mission, presumably with centimeter accuracy [92], will allow researchers to greatly improve the dynamical model of the Sun and the inner Solar system [32,55], including better estimates for $\dot{\mu_\odot}$ and $\dot{G}$.
- Research on a model of Earth tides is needed to unlock the big potential of LLR for estimating the change rate of the gravitational constant.

Author Contributions: Conceptualization, D.P.; methodology, D.P.; software, D.P. and I.D.; validation, D.P. and I.D.; writing, D.P. and I.D. All authors have read and agreed to the published version of the manuscript.

Funding: The research of Dmitry Pavlov was funded by the Russian Science Foundation (project no. 24-22-00391).

Data Availability Statement: The observational data used in this work come from publicly available sources listed in Section 2. Intermediate results of computations are available from authors upon reasonable request.

Acknowledgments: Authors are grateful to Elena Pitjeva (IAA RAS) and Sergey Kurdubov (IAA RAS) for support provided and valuable advice given throughout this work; to Rodolfo Gustavo Cionco (CONICET-UTN) and Marshall Eubanks (Space Initiatives Inc.) for useful references; to Lorenzo Iorio (Ministry of Education and Merit of Italy) for support and encouragement. Planetary observations, including spacecraft ranges which are essential for this work, were collected from the NASA SSD webpage and are supported by Ryan Park, and at the Geoazur website supported by Agnès Fienga. Anonymous reviewers provided useful advice which allowed us to significantly improve the paper.

Conflicts of Interest: The authors declare no conflicts of interest.

Abbreviations

The following abbreviations are used in this manuscript:

ACE	Advanced Composition Explorer
BVLS	Bounded-value least squares
CDDIS	Crustal Dynamics Data Information System
CMB	Cosmic microwave background
CMEs	Coronal mass ejections
CONICET	Consejo Nacional de Investigaciones Científicas y Técnicas (National Scientific and Technical Research Council)
DE	Development Ephmerides
DSN	Deep Space Network
EOP	Earth Orientation Parameters
EPM	Ephemerides of Planets and the Moon
IAA RAS	Institute of Applied Astronomy of the Russian Academy of Sciences
IAU	International Astronomical Union
IERS	International Earth Rotation and Reference Systems Service
LAGEOS	Laser Geodynamics Satellite or Laser Geometric Environmental Observation Survey
LLR	Lunar laser ranging
LOI	Luminosity Oscillations Imager
MESSENGER	Mercury Surface, Space Environment, Geochemistry, and Ranging
MLRS	McDonald Laser Ranging Station
MGS	Mars Global Surveyor
MRO	Mars Reconnaissance Orbiter
NASA JPL	Jet Propulsion Laboratory of the National Aeronautics and Space Administration
POLAC	Lunar Analysis Center of Paris Observatory
SOHO	Solar and Heliospheric Observatory
SLR	Satellite laser ranging
SSD	Solar system dynamics
SWOOPS	Solar Wind Observations Over the Poles of the Sun
TNOs	Trans-Neptunian objects
UTN	Universidad Tecnológica Nacional
VLBI	Very Long Baseline Interferometry
wrms	Weighted root-mean-square residual
WRSS	Weighted Residual Sum of Squares
YAG	Yttrium aluminum garnet

Notes

1 Only Earth–Mars spacecraft ranges are accurate enough and cover a long enough timespan to allow such an estimation.

2 https://ssd.jpl.nasa.gov/?eph_data (accessed on 31 October 2024).

3 http://www.geoazur.fr/astrogeo/?href=observations/base (accessed on 31 October 2024).

4 http://iaaras.ru/en/dept/ephemeris/observations (accessed on 31 October 2024).

5 sftp://gdc.cddis.gsfc.nasa.gov/slr/data/npt_crd (accessed on 31 October 2024).

6 http://polac.obspm.fr/llrdatae.html (accessed on 31 October 2024).

7 https://ssd.jpl.nasa.gov/horizons/ (accessed on 31 October 2024).

8 http://iers.org (accessed on 31 October 2024).

9 However, we must note that the account in [53] of the Sun's mass loss rate $-9 \times 10^{-14} < \dot{M}_\odot / M_\odot < -11 \times 10^{-14}$ was probably inaccurate because it was based on two papers published in 2011 [76] and 2012 [77], well before the end of the MESSENGER observations, and assumed that the activity of the solar wind was similar between consecutive solar cycles, which was not true for solar cycles 23 and 24. The more realistic estimate (8) would result in $\dot{G}$ being zero, assuming the 2σ-bounds of the determined $\dot{\mu}_\odot$, not the 1σ-bounds as claimed in the paper.

References

1. Mohr, P.; Newell, D.; Taylor, B.; Tiesinga, E. CODATA Recommended Values of the Fundamental Physical Constants: 2022. *arXiv* **2024**. [CrossRef]
2. Anderson, J.D.; Schubert, G.; Trimble, V.; Feldman, M.R. Measurements of Newton's gravitational constant and the length of day. *Europhys. Lett.* **2015**, *110*, 10002. [CrossRef]
3. Reasenberg, R.D.; Shapiro, I.I. A radar test of the constancy of the gravitational interaction. In Proceedings of the on the Measurement of Cosmological Variations of the Gravitational Constant, Tallahassee, FL, USA, 12–14 November 1975; Halpern, L., Ed.; University of Florida Press: Tallahassee, FL, USA, 1978; pp. 71–86.
4. Anderson, J.; Keesey, M.; Lau, E.; Standish, E.; Newhall, X. Tests of general relativity using astrometric and radio metric observations of the planets. *Acta Astronaut.* **1978**, *5*, 43–61. [CrossRef]
5. Piteva, E.V. Tests of General Relativity using radar observations of the inner planets. *Byulleten'Instituta Teor. Astron.* **1986**, *15*, 538–543.
6. Pitjeva, E.V.; Pitjev, N.P.; Pavlov, D.A.; Turygin, C.C. Estimates of the change rate of solar mass and gravitational constant based on the dynamics of the Solar System. *Astron. Astrophys.* **2021**, *647*, A141. [CrossRef]
7. Aksim, D.; Pavlov, D. Improving the solar wind density model used in processing of spacecraft ranging observations. *Mon. Not. R. Astron. Soc.* **2022**, *514*, 3191–3201. [CrossRef]
8. Kan, M.; Pavlov, D. Dynamical estimation of masses of the Main asteroid belt and some individual asteroids within the EPM ephemeris using infrared data. In Proceedings of the Astronomy at the Epoch of Multimessenger Studies, Moscow, Russia, 23–28 August 2021; Janus-K; Sternberg Astronomical Institute: Moscow, Russia, 2022; pp. 93–95. [CrossRef]
9. Konopliv, A.S.; Asmar, S.W.; Folkner, W.M.; Karatekin, O.; Nunes, D.C.; Smrekar, S.E.; Yoder, C.F.; Zuber, M.T. Mars high resolution gravity fields from MRO, Mars seasonal gravity, and other dynamical parameters. *Icarus* **2011**, *211*, 401–428. [CrossRef]
10. Yoder, C.F.; Standish, E.M. Martian precession and rotation from Viking lander range data. *J. Geophys. Res. Planets* **1997**, *102*, 4065–4080. [CrossRef]
11. Folkner, W.M.; Yoder, C.F.; Yuan, D.N.; Standish, E.M.; Preston, R.A. Interior Structure and Seasonal Mass Redistribution of Mars from Radio Tracking of Mars Pathfinder. *Science* **1997**, *278*, 1749–1752. [CrossRef]
12. Morley, T.; Budnik, F. Mars Express and Venus Express range residuals for improving planetary ephemerides. In Proceedings of the 21st International Symposium on Space Flight Dynamic, Toulouse, France, 28 September–2 October 2009. Available online: https://issfd.org/ISSFD_2009/OrbitDeterminationI/Morley.pdf (accessed on 29 September 2024).
13. Murphy, T.; Adelberger, E.; Battat, J.; Hoyle, C.; Johnson, N.; McMillan, R.; Stubbs, C.; Swanson, H. APOLLO: Millimeter lunar laser ranging. *Class. Quantum Gravity* **2012**, *29*, 184005. [CrossRef]
14. Murphy, T. Lunar laser ranging: The millimeter challenge. *Rep. Prog. Phys.* **2013**, *76*, 076901. [CrossRef] [PubMed]
15. Colmenares, N.R.; Battat, J.B.R.; Gonzales, D.P.; Murphy, T.W.; Sabhlok, S. Fifteen Years of Millimeter Accuracy Lunar Laser Ranging with APOLLO: Data Reduction and Calibration. *Publ. Astron. Soc. Pac.* **2023**, *135*, 104503. [CrossRef]
16. Chabé, J.; Courde, C.; Torre, J.M.; Bouquillon, S.; Bourgoin, A.; Aimar, M.; Albanèse, D.; Chauvineau, B.; Mariey, H.; Martinot-Lagarde, G.; et al. Recent Progress in Lunar Laser Ranging at Grasse Laser Ranging Station. *Earth Space Sci.* **2020**, *7*, e2019EA000785. [CrossRef]
17. Hugentobler, U.; Neidhardt, A.; Lauber, P.; Ettl, M.; Schreiber, K.U.; Dassing, R.; Klügel, T.; Riepl, S.; Herold, G.; Kronschnabl, G.; et al. The Geodetic Observatory Wettzell—A fundamental reference point. In *Geological Field Trips in Central Western Europe*; Geological Society of America: Boulder, CO, USA, 2011. [CrossRef]
18. Shelus, P.J. MLRS: A lunar/artificial satellite laser ranging facility at the McDonald Observatory. *IEEE Trans. Geosci. Remote Sens.* **1985**, *GE-234*, 385–390. [CrossRef]
19. Bonsack, W.K.; Macknik, L.S.; Dawe, R.S. Lunar and satellite ranging from Haleakala, Maui. *Publ. Astron. Soc. Pac.* **1986**, *98*, 1102.
20. Samain, E.; Mangin, J.; Veillet, C.; Torre, J.M.; Fridelance, P.; Chabaudie, J.; Féraudy, D.; Glentzlin, M.; Pham Van, J.; Furia, M.; et al. Millimetric lunar laser ranging at OCA (Observatoire de la Côte d'Azur). *Astron. Astrophys. Suppl. Ser.* **1998**, *130*, 235–244. [CrossRef]
21. Pitjeva, E.V. Updated IAA RAS planetary ephemerides—EPM2011 and their use in scientific research. *Sol. Syst. Res.* **2013**, *47*, 386–402. [CrossRef]
22. Pitjeva, E.V.; Pitjev, N.P. Development of planetary ephemerides EPM and their applications. *Celest. Mech. Dyn. Astron.* **2014**, *119*, 237–256. [CrossRef]
23. Pavlov, D. Role of lunar laser ranging in realization of terrestrial, lunar, and ephemeris reference frames. *J. Geod.* **2019**, *94*, 5. [CrossRef]
24. Pitjeva, E.; Pavlov, D.; Aksim, D.; Kan, M. Planetary and lunar ephemeris EPM2021 and its significance for Solar system research. *Proc. Int. Astron. Union* **2022**, *15*, 220–225. [CrossRef]
25. Tedesco, E.F.; Noah, P.V.; Noah, M.; Price, S.D. *IRAS Minor Planet Survey V6.0*; Technical Report, NASA Planetary Data System; National Aeronautics and Space Administration: Washington, DC, USA, 2004.
26. Masiero, J.R.; Mainzer, A.K.; Grav, T.; Bauer, J.M.; Cutri, R.M.; Dailey, J.; Eisenhardt, P.R.M.; McMillan, R.S.; Spahr, T.B.; Skrutskie, M.F.; et al. Main Belt asteroids with WISE/NEOWISE. I. Preliminary albedods and diameters. *Astrophys. J.* **2011**, *741*, 68. [CrossRef]

27. Aksim, D.; Pavlov, D. On the Extension of Adams–Bashforth–Moulton Methods for Numerical Integration of Delay Differential Equations and Application to the Moon's Orbit. *Math. Comput. Sci.* **2020**, *14*, 103–109. [CrossRef]
28. Pitjeva, E.V.; Pitjev, N.P. Mass of the Kuiper belt. *Celest. Mech. Dyn. Astron.* **2018**, *130*, 57. [CrossRef]
29. Pavlov, D.; Williams, J.; Suvorkin, V. Determining parameters of Moon's orbital and rotational motion from LLR observations using GRAIL and IERS-recommended models. *Celest. Mech. Dyn. Astron.* **2016**, *126*, 61–88. [CrossRef]
30. Archinal, B.A.; Acton, C.H.; A'Hearn, M.F.; Conrad, A.; Consolmagno, G.J.; Duxbury, T.; Hestroffer, D.; Hilton, J.L.; Kirk, R.L.; Klioner, S.A.; et al. Report of the IAU Working Group on Cartographic Coordinates and Rotational Elements: 2015. *Celest. Mech. Dyn. Astron.* **2018**, *130*, 22. [CrossRef]
31. Folkner, W.; Williams, J.; Boggs, D.; Park, R.; Kuchynka, P. *The Planetary and Lunar Ephemerides DE430 and DE431*; IPN Progress Report 42-196, NASA JPL; National Aeronautics and Space Administration: Washington, DC, USA, 2014.
32. Fienga, A.; Bigot, L.; Mary, D.; Deram, P.; Di Ruscio, A.; Bernus, L.; Gastineau, M.; Laskar, J. Evolution of INPOP planetary ephemerides and Bepi-Colombo simulations. *Proc. Int. Astron. Union* **2022**, *15*, 31–51. [CrossRef]
33. Tian, W. PETREL19: A new numerical solution of planetary and lunar ephemeris. *Celest. Mech. Dyn. Astron.* **2023**, *135*. [CrossRef]
34. Mecheri, R.; Meftah, M. Updated values of solar gravitational moments J2n using HMI helioseismic inference of internal rotation. *Mon. Not. R. Astron. Soc.* **2021**, *506*, 2671–2676. [CrossRef]
35. Lense, J.; Thirring, H. Über den Einfluß der Eigenrotation der Zentralkörper auf die Bewegung der Planeten und Monde nach der Einsteinschen Gravitationstheorie. *Phys. Z.* **1918**, *19*, 156.
36. Everitt, C.W.F.; DeBra, D.B.; Parkinson, B.W.; Turneaure, J.P.; Conklin, J.W.; Heifetz, M.I.; Keiser, G.M.; Silbergleit, A.S.; Holmes, T.; Kolodziejczak, J.; et al. Gravity Probe B: Final Results of a Space Experiment to Test General Relativity. *Phys. Rev. Lett.* **2011**, *106*, 221101. [CrossRef]
37. Everitt, C.W.F.; Muhlfelder, B.; DeBra, D.B.; Parkinson, B.W.; Turneaure, J.P.; Silbergleit, A.S.; Acworth, E.B.; Adams, M.; Adler, R.; Bencze, W.J.; et al. The Gravity Probe B test of general relativity. *Class. Quantum Gravity* **2015**, *32*, 224001. [CrossRef]
38. Pugh, G.E. *Proposal for a Satellite Test of the Coriolis Prediction of General Relativity*; Research Memorandum No. 11; Weapons Systems Evaluation Group, The Pentagon: Washington, DC, USA, 1959.
39. Schiff, L.I. Possible New Experimental Test of General Relativity Theory. *Phys. Rev. Lett.* **1960**, *4*, 215–217. [CrossRef]
40. Petit, G.; Luzum, B. *IERS Conventions 2010 (IERS Technical Note 36)*; Verlag des Bundesamts für Kartographie und Geodäsie: Frankfurt, Germany, 2010.
41. Ciufolini, I.; Paolozzi, A.; Pavlis, E.C.; Ries, J.; Koenig, R.; Matzner, R.; Sindoni, G.; Neumayer, H. Testing gravitational physics with satellite laser ranging. *Eur. Phys. J. Plus* **2011**, *126*, 72. [CrossRef]
42. Ciufolini, I.; Paolozzi, A.; Pavlis, E.C.; Sindoni, G.; Ries, J.; Matzner, R.; Koenig, R.; Paris, C.; Gurzadyan, V.; Penrose, R. An improved test of the general relativistic effect of frame-dragging using the LARES and LAGEOS satellites. *Eur. Phys. J. C* **2019**, *79*. [CrossRef]
43. Iorio, L. Some considerations on the present-day results for the detection of frame-dragging after the final outcome of GP-B. *Europhys. Lett.* **2011**, *96*, 30001. [CrossRef]
44. Ries, J.C.; Ciufolini, I.; Pavlis, E.C.; Paolozzi, A.; Koenig, R.; Matzner, R.A.; Sindoni, G.; Neumayer, H. The Earth's frame-dragging via laser-ranged satellites: A Response to "Some considerations on the present-day results for the detection of frame-dragging after the final outcome of GP-B" by Iorio L. *Europhys. Lett.* **2011**, *96*, 30002. [CrossRef]
45. Renzetti, G. Some reflections on the Lageos frame-dragging experiment in view of recent data analyses. *New Astron.* **2014**, *29*, 25–27. [CrossRef]
46. Iorio, L. Limitations in Testing the Lense–Thirring Effect with LAGEOS and the Newly Launched Geodetic Satellite LARES 2. *Universe* **2023**, *9*, 211. [CrossRef]
47. Iorio, L. Juno, the angular momentum of Jupiter and the Lense–Thirring effect. *New Astron.* **2010**, *15*, 554–560. [CrossRef]
48. Finocchiaro, S.; Iess, L.; Folkner, W.M.; Asmar, S. The Determination of Jupiter's Angular Momentum from the Lense–Thirring Precession of the Juno Spacecraft. In Proceedings of the AGU Fall Meeting Abstracts, San Francisco, CA, USA, 5–9 December 2011; Volume 2011, p. P41B-1620.
49. Durante, D.; Cappuccio, P.; di Stefano, I.; Zannoni, M.; Casajus, L.G.; Lari, G.; Falletta, M.; Buccino, D.R.; Iess, L.; Park, R.S.; et al. Testing General Relativity with Juno at Jupiter. *Astrophys. J.* **2024**, *971*, 145. [CrossRef]
50. Iorio, L. Is it possible to measure the Lense-Thirring effect on the orbits of the planets in the gravitational field of the Sun? *Astron. Astrophys.* **2005**, *431*, 385–389. [CrossRef]
51. Iorio, L. Constraining the Angular Momentum of the Sun with Planetary Orbital Motions and General Relativity. *Sol. Phys.* **2012**, *281*, 815–826. [CrossRef]
52. Park, R.S.; Folkner, W.M.; Konopliv, A.S. Estimation of Solar Angular Momentum from Lense–Thirring Precession of Mercury. In Proceedings of the IAU General Assembly, Honolulu, HI, USA, 3–14 August 2015; Volume 29, p. 2227771.
53. Genova, A.; Mazarico, E.; Goossens, S.; Lemoine, F.G.; Neumann, G.A.; Smith, D.E.; Zuber, M.T. Solar system expansion and strong equivalence principle as seen by the NASA MESSENGER mission. *Nat. Commun.* **2018**, *9*, 289. [CrossRef] [PubMed]
54. Pavlov, D.; Dolgakov, I. General relativity tests by the dynamics of the Solar system. In *Proceedings of the Journées 2023 "Systèmes de Référence Spatio-Temporels"*; Bizouard, C., Fienga, A., Paganelli, F., Eds.; Observatoire de la Côte d'Azur: Nice, France, 2024; pp. 156–160.

55. Iorio, L. Analytically calculated post-Keplerian range and range-rate perturbations: The solar Lense–Thirring effect and BepiColombo. *Mon. Not. R. Astron. Soc.* **2018**, *476*, 1811–1825. [CrossRef]
56. Pijpers, F.P. Helioseismic determination of the solar gravitational quadrupole moment. *Mon. Not. R. Astron. Soc.* **1998**, *297*, L76–L80. [CrossRef]
57. Prša, A.; Harmanec, P.; Torres, G.; Mamajek, E.; Asplund, M.; Capitaine, N.; Christensen-Dalsgaard, J.; Depagne, É.; Haberreiter, M.; Hekker, S.; et al. Nominal values for selected solar and planetary quantities: IAU 2015 Resolution B3. *Astron. J.* **2016**, *152*, 41. [CrossRef]
58. Fröhlich, C.; Lean, J. Solar radiative output and its variability: Evidence and mechanisms. *Astron. Astrophys. Rev.* **2004**, *12*, 273–320. [CrossRef]
59. Wu, C.-J.; Krivova, N.A.; Solanki, S.K.; Usoskin, I.G. Solar total and spectral irradiance reconstruction over the last 9000 years. *Astron. Astrophys.* **2018**, *620*, A120. [CrossRef]
60. Mishra, W.; Srivastava, N.; Wang, Y.; Mirtoshev, Z.; Zhang, J.; Liu, R. Mass loss via solar wind and coronal mass ejections during solar cycles 23 and 24. *Mon. Not. R. Astron. Soc.* **2019**, *486*, 4671–4685. [CrossRef]
61. Shoda, M.; Cranmer, S.R.; Toriumi, S. Formulating Mass-loss Rates for Sun-like Stars: A Hybrid Model Approach. *Astrophys. J.* **2023**, *957*, 71. [CrossRef]
62. Boro Saikia, S.; Jin, M.; Johnstone, C.P.; Lüftinger, T.; Güdel, M.; Airapetian, V.S.; Kislyakova, K.G.; Folsom, C.P. The solar wind from a stellar perspective - How do low-resolution data impact the determination of wind properties? *Astron. Astrophys.* **2020**, *635*, A178. [CrossRef]
63. Cranmer, S.R. Mass-loss Rates from Coronal Mass Ejections: A Predictive Theoretical Model for Solar-type Stars. *Astrophys. J.* **2017**, *840*, 114. [CrossRef]
64. Kuchynka, P.; Folkner, W.M.; Konopliv, A.S. *Station-Specific Errors in Mars Ranging Measurements*; Interplanetary Network Progress Report 42-190, NASA JPL; National Aeronautics and Space Administration: Washington, DC, USA, 2012. Available online: https://ipnpr.jpl.nasa.gov/progress_report/42-190/190C.pdf (accessed on 29 September 2024).
65. Asmar, S.W. *Radio Science Techniques for Deep Space Exploration*; JPL Deep-Space Communications and Navigation; John Wiley & Sons: Hoboken, NJ, USA, 2022.
66. Solomon, S.C.; McNutt, R.L.; Gold, R.E.; Acuña, M.H.; Baker, D.N.; Boynton, W.V.; Chapman, C.R.; Cheng, A.F.; Gloeckler, G.; Head III, J.W.; et al. The MESSENGER mission to Mercury: Scientific objectives and implementation. *Planet. Space Sci.* **2001**, *49*, 1445–1465. [CrossRef]
67. Radomski, M.S.; Doll, C.E. Differenced Range Versus Integrated Doppler (DRVID) Ionospheric Analysis of Metric Tracking in the Tracking and Data Relay Satellite System (TDRSS). In Proceedings of the Flight Mechanics/Estimation Theory Symposium, NASA, Greenbelt, MD, USA, 16–18 May 1995; pp. 31–45.
68. Gizon, L.; Appourchaux, T.; Gough, D. LOI/SOHO Constraints on Oblique Rotation of the Solar Core. *Symp. Int. Astron. Union* **1998**, *185*, 37–40. [CrossRef]
69. Bai, T.; Sturrock, P.A. Evidence for a fundamental period of the sun and its relation to the 154 day complex of periodicities. *Astrophys. J.* **1993**, *409*, 476. [CrossRef]
70. Bellinger, E.P.; Christensen-Dalsgaard, J. Asteroseismic Constraints on the Cosmic-time Variation of the Gravitational Constant from an Ancient Main-sequence Star. *Astrophys. J. Lett.* **2019**, *887*, L1. [CrossRef]
71. Alvey, J.; Sabti, N.; Escudero, M.; Fairbairn, M. Improved BBN constraints on the variation of the gravitational constant. *Eur. Phys. J. C* **2020**, *80*, 148. [CrossRef]
72. Zhu, W.W.; Desvignes, G.; Wex, N.; Caballero, R.N.; Champion, D.J.; Demorest, P.B.; Ellis, J.A.; Janssen, G.H.; Kramer, M.; Krieger, A.; et al. Tests of gravitational symmetries with pulsar binary J1713+0747. *Mon. Not. R. Astron. Soc.* **2018**, *482*, 3249–3260. [CrossRef]
73. Bonanno, A.; Fröhlich, H.E. A New Helioseismic Constraint on a Cosmic-time Variation of G. *Astrophys. J. Lett.* **2020**, *893*, L35. [CrossRef]
74. Le, T.D. A study of space–time variation of the gravitational constant using high-resolution quasar spectra. *Gen. Relativ. Gravit.* **2021**, *53*, 37. [CrossRef]
75. Le, T.D. Exploring secular variation of the gravitational constant from high-resolution quasar spectra. *Sci. Rep.* **2024**, *14*, 15610. [CrossRef] [PubMed]
76. Pinto, R.F.; Brun, A.S.; Jouve, L.; Grappin, R. Coupling the solar dynamo and the corona: Wind properties, mass, and momentum losses during an activity cycle. *Astrophys. J.* **2011**, *737*, 72. [CrossRef]
77. Pitjeva, E.V.; Pitjev, N.P. Changes in the Sun's mass and gravitational constant estimated using modern observations of planets and spacecraft. *Sol. Syst. Res.* **2012**, *46*, 78–87. [CrossRef]
78. Pitjeva, E.V.; Pitjev, N.P. Masses of the Main Asteroid Belt and the Kuiper Belt from the Motions of Planets and Spacecraft. *Astron. Lett.* **2018**, *44*, 554–566. [CrossRef]
79. Liu, S.; Fienga, A.; Yan, J. A ring model of the main asteroid belt for planetary ephemerides. *Icarus* **2022**, *376*, 114845. [CrossRef]
80. Antia, H.M.; Chitre, S.M.; Gough, D.O. Temporal variations in the Sun's rotational kinetic energy. *Astron. Astrophys.* **2008**, *477*, 657–663. [CrossRef]
81. Farinella, P.; Froeschlé, C.; Froeschlé, C.; Gonczi, R.; Hahn, G.; Morbidelli, A.; Valsecchi, G.B. Asteroids falling into the Sun. *Nature* **1994**, *371*, 314–317. [CrossRef]

82. Pitjeva, E.; Pavlov, D.; Aksim, D.; Kan, M.; Dolgakov, I. EPM2021 and EPM2021H. 2021. Available online: https://iaaras.ru/en/dept/ephemeris/epm/2021/ (accessed on 31 October 2024).
83. Farinella, P.; Davis, D.R. Collision rates and impact velocities in the main asteroid belt. *Icarus* **1992**, *97*, 111–123. [CrossRef]
84. Vokrouhlický, D.; Farinella, P.; Bottke, W.F. The Depletion of the Putative Vulcanoid Population via the Yarkovsky Effect. *Icarus* **2000**, *148*, 147–152. [CrossRef]
85. Weber, E.J.; Davis, L.J. The Angular Momentum of the Solar Wind. *Astrophys. J.* **1967**, *148*, 217–227. [CrossRef]
86. Finley, A.J.; Deshmukh, S.; Matt, S.P.; Owens, M.; Wu, C.J. Solar Angular Momentum Loss over the Past Several Millennia. *Astrophys. J.* **2019**, *883*, 67. [CrossRef]
87. Finley, A.J.; Hewitt, A.L.; Matt, S.P.; Owens, M.; Pinto, R.F.; Réville, V. Direct Detection of Solar Angular Momentum Loss with the Wind Spacecraft. *Astrophys. J. Lett.* **2019**, *885*, L30. [CrossRef]
88. Ruggiero, M.L.; Iorio, L. Gravitomagnetic time-varying effects on the motion of a test particle. *Gen. Relativ. Gravit.* **2010**, *42*, 2393–2402. [CrossRef]
89. Agazie, G.; Anumarlapudi, A.; Archibald, A.M.; Arzoumanian, Z.; Baker, P.T.; Bécsy, B.; Blecha, L.; Brazier, A.; Brook, P.R.; Burke-Spolaor, S.; et al. The NANOGrav 15 yr Data Set: Evidence for a Gravitational-wave Background. *Astrophys. J. Lett.* **2023**, *951*, L8. [CrossRef]
90. Pokorný, P.; Janches, D.; Sarantos, M.; Szalay, J.R.; Horányi, M.; Nesvorný, D.; Kuchner, M.J. Meteoroids at the Moon: Orbital properties, surface vaporization, and impact ejecta production. *J. Geophys. Res. Planets* **2019**, *124*, 752–778. [CrossRef]
91. Williams, J.G.; Boggs, D.H.; Folkner, W.M. *DE430 Lunar Orbit, Physical Librations, and Surface Coordinates*; Jet Propulsion Laboratory Interoffice Memorandum 335-JW, DB, WF-20130722-016; California Institute of Technology: Pasadena, CA, USA, 2013. Available online: https://naif.jpl.nasa.gov/pub/naif/generic_kernels/spk/planets/de430_moon_coord.pdf (accessed on 31 October 2024).
92. Paik, M.; Asmar, S.; Border, J.; Shin, D.K.; Martinez, G.; Lippincott, J.; Angkasa, K.S.; Bedrossian, A.; Iess, L.; Cappuccio, P. Centimeter-Level Ranging Results from the 2022 BepiColombo Solar Conjunction. In Proceedings of the AGU Fall Meeting, Chicago, IL, USA, 12–16 December 2022; p. P42G-2483.

Disclaimer/Publisher's Note: The statements, opinions and data contained in all publications are solely those of the individual author(s) and contributor(s) and not of MDPI and/or the editor(s). MDPI and/or the editor(s) disclaim responsibility for any injury to people or property resulting from any ideas, methods, instructions or products referred to in the content.